photonics

MDPI

Article

Optimal Scanning Pattern for Initial Free-Space Optical-Link Alignment

Petr Skryja and Peter Barcik *

Department of Radioelectronics, Brno University of Technology, 616 00 Brno, Czech Republic; xskryj01@vutbr.cz
* Correspondence: barcik@vut.cz

Abstract: Since free-space optical links (especially fully photonic ones) are very challenging to accurately align; scanning algorithms are used for the initial search and alignment of the transceivers. The initial alignment aims to intercept the optical beam so that it hits a position-sensitive detector. However, this operation can be very time-consuming (depending on the system parameters, such as transceiver parameters, distance between transceivers, divergence of the transmitter, angle of view of the receiver, etc.). A spiral scan is used as the most widespread pattern for scanning. This article examines the effects of system parameters (e.g., global navigation satellite systems and compass accuracy) on the angular area of uncertainty that must be scanned to find the optical beam. Furthermore, several types of spiral pattern are compared depending on the time of the scan execution and the required number of points for scanning the given uncertainty area. The cut hexagonal spiral scan achieved the best results as it required 18.1% less time than the common spiral scan for the presented transceiver.

Keywords: FSO; spiral scan; spiral patterns; alignment; angular area of uncertainty

1. Introduction

The aim of the emerging 6G architecture is for it to be flexible, efficient, and capable of integrating diverse elements such as networks, joint communication and sensing, non-terrestrial and terrestrial communication, AI-powered enablers, and distributed computing capabilities [1,2]. The progress of 6G will be shaped by a range of innovative technologies, and smart optical transport connectivity is one such technology that will play a significant role [3,4]. Free-Space Optics (FSO) technology can serve as a complement to Radio-Frequency (RF) technology, reducing congestion in the radio frequency part of the spectrum [5,6]. The FSO systems must be constantly improved to meet the conditions for implementation in modern mobile networks. Thanks to the implementation of new photonic technologies, optomechanical devices and Artificial Intelligence (AI) solutions, the individual subsystems of FSO transceivers, such as pointing and tracking, are continuously being enhanced. Improving these subsystems is the subject of research by many scientific groups [7–13].

In FSO systems, accurate pointing, acquisition, and tracking are crucial for reliable communication, especially for links in which the received optical wave is coupled directly into the optical fiber. Firstly, the link must be coarsely aligned so that the transmitted optical beam falls within the angular area of the uncertainty of the receiver. Consequently, scanning techniques are typically employed to locate the counterpart optical transmitter within this area. This ambiguity arises due to factors such as the accuracy of electrical and mechanical components, limited precision of navigation devices, etc. This procedure is typically time-consuming and requires careful adjustments. In the process of locating the optical transmitter, the scanning algorithm, often employing spiral movement patterns, systematically explores the angular area of uncertainty. The spiral scanning algorithm starts from the center of the search area and progressively moves to the outer edges. By following

check for updates

Citation: Skryja, P.; Barcik, P. Optimal Scanning Pattern for Initial Free-Space Optical-Link Alignment. *Photonics* **2024**, *11*, 540. https://doi.org/10.3390/photonics11060540

Received: 24 April 2024
Revised: 31 May 2024
Accepted: 3 June 2024
Published: 5 June 2024

this pattern, the receiver is able to capture and acquire the optical signal transmitted by the transmitter. During the scanning process, the Position-Sensitive Detector (PSD) (e.g., four-quadrant photodiode) detects the incident light from the transmitter and ends the scanning process if the defined threshold of optical power is exceeded. After this, the system passes into the tracking state and, based on the obtained position of the spot from the PSD, continuously compensates for the misalignment so that the beam hits a certain point on the PSD (mostly the center of the detector).

The novelty of this paper lies in specifying the angular area of uncertainty for auto-aligning the FSO transceiver (which uses a global navigation satellite system and compass) and comparing a suitable spiral scan pattern to optimize the required time for optical beam acquisition during the initial alignment of the transceivers. The results of this paper can speed up the reconfiguration of the free-space optical network, for example, to maintain communication in degraded weather conditions.

The paper is structured as follows. The next section presents a review of current research dealing with FSO acquisition and alignment strategies from different perspectives. Section 3 provides a brief overview of the FSO transceiver system used for the implementation of the investigated scanning methods. Section 4 discusses determining the angular area of uncertainty that needs to be scanned. Section 5 presents the optimal spiral scan for transmitter beam acquisition. Section 6 compares the scan patterns in terms of the required execution time and number of points. The last section concludes the paper.

2. Related Works

Modern communication services require higher data throughput and at the same time create a higher dependence on the stability and availability of the network infrastructure. Network outages can result in loss of data or financial gain. Outages can be caused, for example, by network design errors, human failures, or unpredictable natural disasters. In such situations, the goal is to restore operations or smoothly and quickly switch to a backup route. FSO technology can serve as an emergency communication system and can be included in the disaster network resilience program. The optimal placement of FSO transceivers in a natural disaster is described in [14]. The authors were concerned with minimizing the number of transceivers needed to restore the network and took into account dependence on the weather to find strategic locations to guarantee a given network throughput. The designed solution (network) can reconfigure itself depending on the weather conditions. Reconfiguration, however, requires the acquisition and pointing of the FSO transceiver, which can delay the installation of the entire communication network.

The authors in article [15] deal with acquisition, pointing, and tracking for ground-satellite links. They consider that the angular area of uncertainty is typically larger than the beam divergence required for detection. However, a large angular area of uncertainty with a narrow beam divergence can lead to an unreasonably long acquisition time. Angular area of uncertainty is given by a combination of altitude, azimuth, elevation, and gimbal uncertainties. For beam acquisition, continuous spiral, step (square) spiral, segmented scan, and raster scan are introduced. Among these, continuous spiral scan is considered the most efficient, while raster scan is regarded as less efficient. Acquisition approaches stare/stare, stare/scan, scan/stare, and scan/scan are discussed in terms of the receiver's field of view, the distance between transceivers, and acquisition probability. The stare/scan technique is concluded as being well suited for ground-to-satellite systems. Furthermore, power criteria and the impact of four-quadrant photodiode noise are described.

Article [16] discusses various types of acquisition, pointing, and tracking mechanisms, including gimbal-based, mirror-based, gimbal–mirror hybrid, adaptive optics, liquid crystal, RF–FSO hybrid, and other mechanisms. The authors compared these mechanisms in relation to pointing resolution, angular steering speed, and application. Mirror-based, adaptive optics and RF–FSO hybrid mechanisms are highlighted as viable options for building-to-building communications. Additionally, for unmanned aerial vehicles or autonomous transceivers, the use of a gimbal-based mechanism is advised.

Paper [17] introduces a beacon-less acquisition approach utilizing the spiral scanning method. The system uses a gimbal mechanism combined with a fast-steering mirror and a Complementary Metal-Oxide Semiconductor (CMOS) image sensor. The proposed method combines the utilization of a gimbal and a fast-steering mirror for beam acquisition. During the process, the spiral scan is performed by employing both the gimbal and the mirror. This approach involves conducting an additional scan using the fast-steering mirror at each spiral point of the gimbal. By doing so, the method expands the field of view of the gimbal and reduces the number of spiral scan points required.

A novel approach to the analytical optimization of spatial acquisition for inter-satellite optical communication is presented in [18]. The authors deal with mean acquisition time estimation, where a spiral is used as a scanning pattern. The optimum ratio between the angular area of uncertainty and pointing-error deviation is found to be 3.

The impact of atmospheric turbulence on the optical beam is described in article [19]. It can be seen that the atmospheric turbulences create fluctuations in optical intensity and at the same time cause random deviation of the optical beam position, which is called beam wandering. These phenomena can increase the angular area of uncertainty and thus the time required for scanning and sampling during acquisition.

An autoaligning FSO module is presented in [20], where the authors used a phototransistor ring in combination with a Charge Coupled Device (CCD) sensor. This module uses a simple row scan for beam acquisition, where information from the optical beam of the CCD sensor, the signal from the phototransistor sensor, the signal from the photodiode, and the current position of the servomechanisms are taken into account for pointing purposes. Furthermore, the system was tested for its ability to suppress vibrations.

Two acquisition/alignment methods are presented in [21]. The first one is a black-box AI-based algorithm used with a gimbal-based mechanism (the algorithm does not have any information about the system). The algorithm uses Particle-Swarm Optimization (PSO) to find the beam position that returns the highest received power. The authors investigated swarm sizes in order to minimize the convergence (alignment) time. In the described experiment, this method achieved a pointing success rate of 96%. The second one is a multi-stage Greedy algorithm (partial information about the system is known). This algorithm assumes that the aligning problem is characterized by a well-behaved global minimum and that the optimization gradient is circularly symmetric around it. Furthermore, a characteristic of received optical power as a function of the x and y coordinates of the used stepper motors is available for adaptive step size control. The greedy algorithm provides a faster convergence to maximum optical power than the previously mentioned AI-based algorithm. However, the pointing success rate of this algorithm was (according to the experiment) 92%.

In Ref. [22], a hexagonal scanning method for satellite laser communication is modelled. The hexagonal scan is divided into inner and outer parts. The authors compare this method to their original hexagonal scan and demonstrate that the required scan time is reduced by 6.4%.

Article [23] deals with the acquisition of a moving target. The rectangular spiral scan, hexagonal spiral scan, and hexagonal honeycomb scan methods are compared here. The hexagonal honeycomb scan proposed by the authors achieves a 3% higher acquisition probability than a non-hexagonal scan.

In Ref. [24], the authors present the use of a spiral scan (instead of a raster one) for use in an Atomic Force Microscope (AFM). The principle is very similar to scanning the area of uncertainty in FSO since a Micro-Electromechanical System (MEMS) and a photodiode are used here. The described method focuses on cross-coupling and vibration issues to improve the imaging performance of an AFM at higher than normal scanning speeds.

A novel pointing-and-acquisition algorithm for bidirectional FSO communications between a gateway and an aircraft was proposed in [25]. An RF signal is used to exchange Global Navigation Satellite System (GNSS) information and angle-of-arrival estimation (by using a planar or lens antenna array). This information is used for open-loop coarse point-

ing, in which a beacon laser at the aircraft is replaced with multiple passive retroreflectors, reflecting the uplink beacon beam back to the gateway.

The authors in [26] investigate the Average Acquisition Probability (AAP) calculation method for spiral-circular composite scanning suitable for communication between satellites. An effective coverage area and acquisition probability are calculated. The AAP was developed to describe the influence of the field of uncertainty and vibration simultaneously. With the help of the presented calculation method, optimal system parameters can be determined.

An acquisition, tracking, and pointing system based on computer vision for reconfigurable FSO communication systems is presented in [27]. The receiver is marked by a landmark to estimate the direction and relative position from the transceiver by applying image recognition and computer vision techniques. Further trade-offs among field of view, latency, and reliability are analyzed and the experimental results of measurement on FSO with an effective range of 12 m are presented. The proposed method can recognize and track a moving target at a speed of 0.15 m/s and support 10 Mbps communication.

3. FSO Transceiver System Description

The scan methods examined and presented in this paper were investigated to support an auto-aligning short-range transceiver, the description of which will follow. The layout of the transceiver is shown in Figure 1a. The system consists of three main parts. The first part is the altazimuth mount, which allows rotations in azimuthal and elevational directions. The resolution of the rotation is 1 μrad. The second part consists of the optical components of the transceiver. The transceiver uses two optical channels. For initial/coarse pointing, a channel with a850 nm laser diode is used as a beacon, whose divergence is set using a lens. For reception/positional detection of the counterpart's navigation beam, a four-quadrant photodiode with a receiving lens is used. The second channel is used for communication and uses a 1550 nm laser beam. The transmitting data is carried by an optical cable through an Erbium-Doped Fiber Amplifier (EDFA), which is used to increase optical power to support data transmission ranges up to 1 km. From the EDFA, the optical signal is guided in an optical fiber to the collimator, which collimates the beam and allows setting the required divergence. A Schmidt–Cassegrain telescope with adjustable focus is used for receiving the communication beam from the counterpart transmitter. This telescope focuses the beam onto an MEMS mirror, from where it is reflected into the receiving optical fiber. The MEMS mirror is used together with another four-quadrant photodiode to compensate for atmospheric phenomena affecting the receiving communication beam. The last part creates a controlling unit used to control the altazimuth mount, optical components, pointing, acquisition, and tracking. This part also includes a GNSS and a digital compass module.

To point/align two such transceivers, an initial pointing is performed by calculation of the bearing (angle rotation to the north) and elevation angles for each transceiver and their required rotation angles to these positions. Bearing and elevation are calculated by obtained positions from GNSS (latitude + longitude + altitude) and compass (actual bearing + actual elevation), which exchange transceivers with each other by using LoRa module in peer-to-peer mode. After this step, the transceivers should be aligned, but GNSS and compass accuracy will cause the incorrect calculation of bearing and elevation angles. Furthermore, the accuracy of the gimbal and beam detection sensor will also impact the final positional error. The mentioned accuracies define the angular area of uncertainty, Θ_{unc}, which, after the initial pointing, needs to be scanned to find (detect) the optical beam of the opposite transceiver.

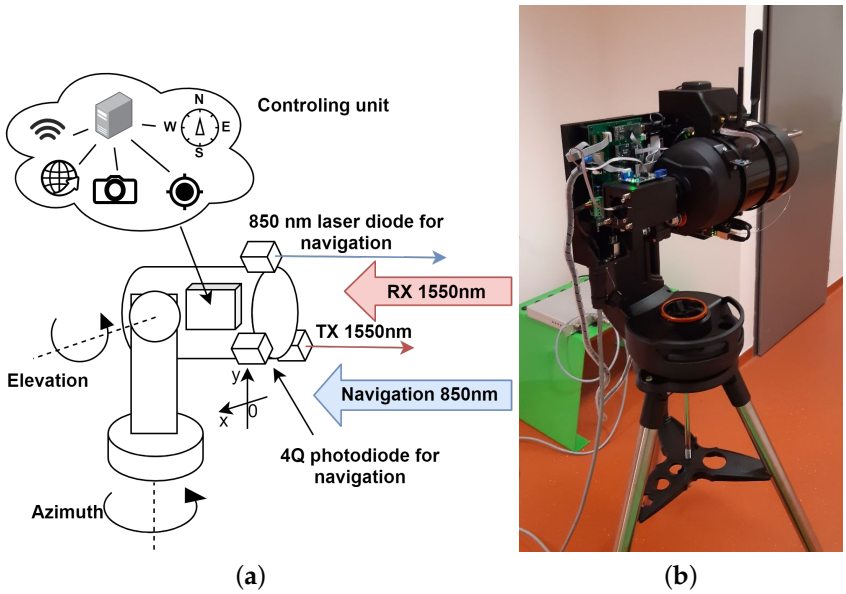

Figure 1. (**a**) FSO transceiver layout. (**b**) FSO transceiver prototype during measurement.

4. Determination of the Angular Area of Uncertainty

The accuracy of GNSS has an impact on the correct calculation of the horizontal distance of the transceivers, L, and their bearing angle. In Figure 2, a corner case, where the GNSS error reaches the highest deviation in the direction perpendicular to the transceiver link, is shown. In this case, the calculation of the horizontal distance is affected by the error

$$\Delta L_{gnss} = L' - L = \frac{2\ gnss\_error}{sin(\beta_{gnss})} - L \tag{1}$$

and the bearing angle by error

$$\beta_{gnss} = arctan\left(\frac{2\ gnss\_error}{L}\right), \tag{2}$$

where the $gnss\_error$ is defined by the GNSS accuracy.

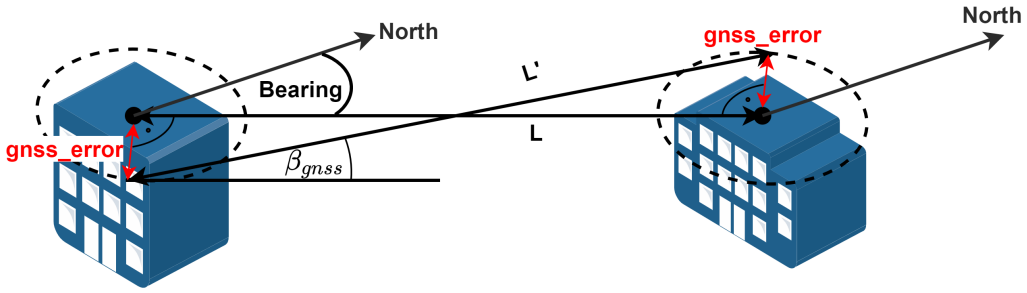

Figure 2. Angle error β_{gnss} and horizontal distance error caused by GNSS accuracy.

The second corner case only affects the incorrect calculation of the horizontal distance, L, since the β_{gnss} angle is equal to zero, as shown in Figure 3. The horizontal incorrect distances are then given as $L'' = L - 2gnss\_error$ and $L''' = L + 2gnss\_error$.

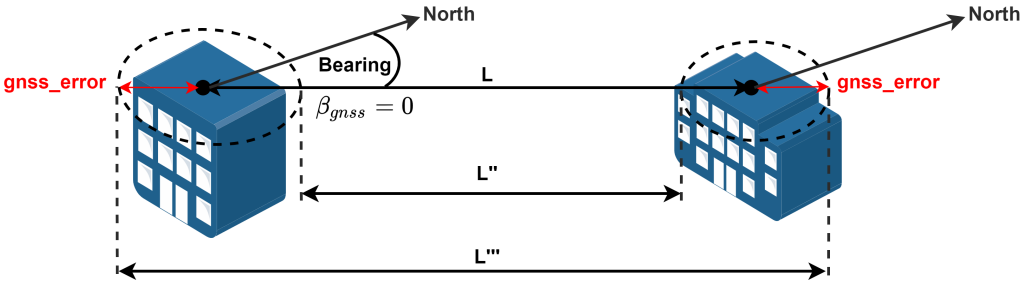

Figure 3. Distance error caused by GNSS accuracy for $\beta_{gnss} = 0$.

The accuracy of the altitude measurement affects the error of elevation angle and line of sight calculation. Figure 4 shows the corner cases of elevation angle β_{El} calculation affected by altitude error Alt_error. The error of the elevation angle is defined by

$$\beta'_{El} = \alpha'_{El} - \alpha_{El}, \tag{3}$$

$$\beta''_{El} = \alpha''_{El} - \alpha_{El}, \tag{4}$$

respectively, where α_{El} is the elevation angle,

$$\alpha_{El} = arctan\left(\frac{\Delta_{alt}}{L}\right), \tag{5}$$

where $\Delta_{alt} = Alt_1 - Alt_2$ is the altitude difference of the transceivers and L is the distance of the transceivers. The angles

$$\alpha'_{El} = arctan\left(\frac{\Delta_{alt} + 2Alt\_error}{L}\right) \tag{6}$$

$$\alpha''_{El} = arctan\left(\frac{\Delta_{alt} - 2Alt\_error}{L}\right) \tag{7}$$

define the corner cases for maximum altitude errors $+Alt\_error$ and $-Alt\_error$.

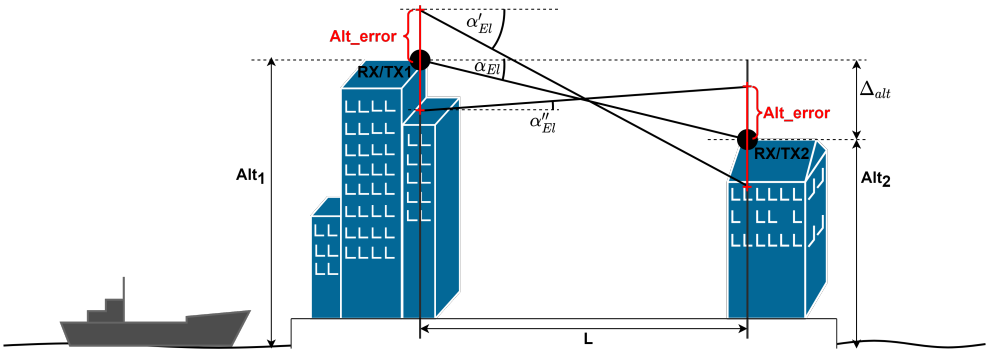

Figure 4. Elevation angle error affected by altitude accuracy.

The angular area of the uncertainty of the presented transceiver is also affected by the accuracy of the compass (bearing and elevation angle sensor). The accuracy of the sensor depends on the presence of metal parts and magnetic sources near the sensor. Also, to meet the accuracy specified by the manufacturer it is usually necessary to calibrate the sensor by moving and rotating it in random directions.

Last but not least, the pointing accuracy depends on the resolution capabilities of the altazimuth mount (gimbal). However, the used mount achieves high accuracy in the order of µrad, and thus its influence on the initial/rough pointing can be neglected.

Overall, the error angles β_{gnss} and β_{El} reach the highest error at short distances and decrease exponentially with increasing distance. The biggest elevation error, β_{El}, occurs when the transmitter and receiver are placed at the same altitude (Δ_{alt} = 0 m). A lower elevation error is achieved with a higher absolute value of Δ_{alt}, mainly for short distances. For longer distances, the impact of Δ_{alt} can be neglected. The impact of distance error ΔL is in the order of centimeters for common GNSS accuracies (*gnss_err* in the order of meters) and distances L > 100 m. For this reason, the influence of the distance error ΔL to the elevation angle α_{El} can be neglected because it will be much lower compared to the error caused by altitude inaccuracy. At large distances, therefore, the compass accuracy will have the greatest influence on the angular size of the angular area of uncertainty. The influence of GNSS accuracy can be further reduced many times by using Real Time Kinematic (RTK) technology, which uses knowledge of the position of reference stations and, by calculating the differential correction, can increase the accuracy of determining the position up to 1 cm. The resulting angular area of uncertainty is then mainly determined by the combination of the errors described above as

$$\Theta_{unc} = 2 \cdot \max\Big(\max\Big(\beta_{gnss}, \beta_{bearing}\Big), \max\big(|\beta'_{El}|, |\beta''_{El}|, \beta_{elevation}\big)\Big), \tag{8}$$

where the function max() takes the bigger of the specified parameters and $\beta_{bearing}$ and $\beta_{elevation}$ are the compass accuracies declared by the manufacturer.

5. Optimal Spiral Scan Pattern for Acquisition

As mentioned in the introduction, a spiral scan is most widely used in FSO. The calculation of spiral points (coordinates) for sampling the angular area of uncertainty can be done using the polar equation of the spiral with arc approximation,

$$r_i = \frac{\varphi_{FRS}(1 - F_o)}{2\pi}\varphi_i, \tag{9}$$

where r_i is the radial distance of point i from the center of the spiral, φ_i is an angle rotation of the point i, F_o is an overlap factor, and φ_{FRS} is a spiral step for each (2π rad) rotation, defined as

$$\varphi_{FRS} = \Theta_{AOV}(1 - F_o), \tag{10}$$

where Θ_{AOV} is the angle of view of the receiver. The algorithm for obtaining a point $i > 0$ on a spiral uses the equation

$$\varphi_i = \varphi_{i-1} + \frac{Arc_{step}}{r_{i-1}}. \tag{11}$$

The position of an initial point $i = 0$ can be choosed as $r_0 = \varphi_{FRS}/2$, $\varphi_0 = 0$ and $Arc_{step} = \varphi_{FRS}$. The parameters of the spiral are shown in Figure 5. The algorithm is stopped at the condition when $\varphi_i > \varphi_{max}$, where

$$\varphi_{max} = N_{rings} 2\pi \tag{12}$$

defines the maximum angle of the spiral rotation to cover the angular area of uncertainty of radius Θ_{unc} and

$$N_{rings} = \frac{\Theta_{unc}}{2\varphi_{FRS}} \tag{13}$$

gives a number of spiral rings. The number of loops of the algorithm finally indicates the number of points, i_{max}, that make up the spiral.

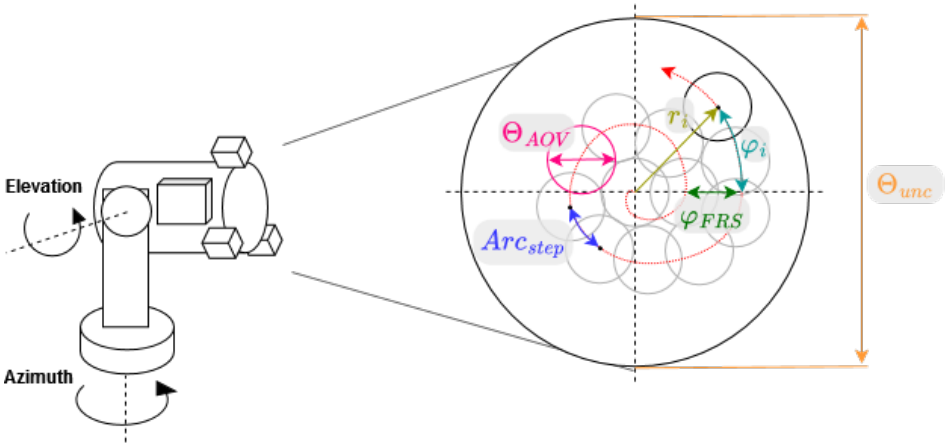

Figure 5. Parameters of the spiral.

In Figure 6a, a spiral scan is depicted. The red dashed circle defines the angular area of uncertainty, Θ_{unc}, the black solid circles correspond to the receiver angle of view, Θ_{AOV}, and the blue solid line shows a path between points that starts at the coordinates (0, 0). Further scan charts will use the same terminology. From Figure 6a, it can be seen that the algorithm for spiral generation suffers from unfilled spaces around the center. This can be improved by adding a few more points near the center, as shown in Figure 6b. This can be done by using the algorithm for a spiral, where $Arc_{step} = r_0 = \varphi_{FRS}/2.5$.

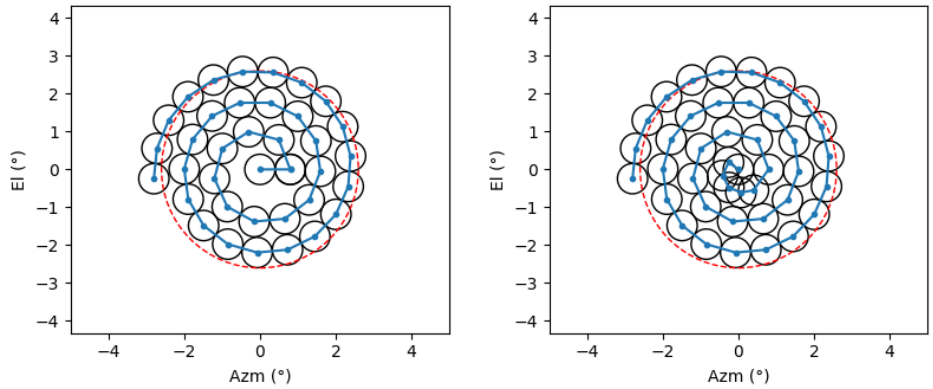

(**a**) (**b**)

Figure 6. (**a**) Spiral scan. (**b**) Spiral scan with additional infill around center.

Figure 7a shows a square spiral scan that starts at the coordinates (0, 0) and advances in a direction from this point with an azimuthal step,

$$\Delta Azm = \pm\varphi_{FRS}, \tag{14}$$

and elevational step,

$$\Delta El = \pm\varphi_{FRS}. \tag{15}$$

However, this scan contains several points that are mostly outside the angular area of uncertainty, and there is very little probability of finding a beam spot at these points. Therefore, these points can be removed to speed up the scan, as shown in Figure 7b. Better results can also be further achieved by rotating the entire scan by 45 degrees, as shown in Figure 7c, where between most of the scan points there is a movement in a diagonal direction, which engages both gimbal motors (azimuthal and elevational) equally and leads to the most time-efficient movement.

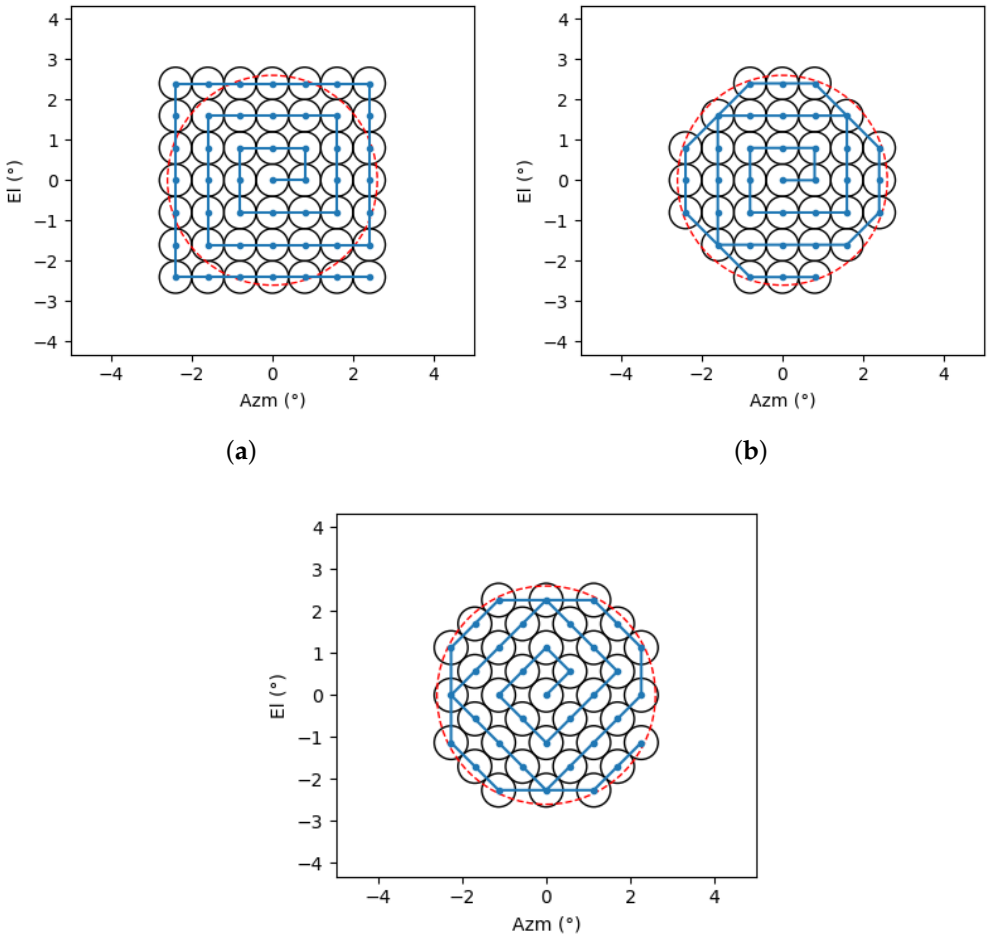

Figure 7. (**a**) Square spiral scan. (**b**) Cut square spiral scan. (**c**) Cut square spiral scan rotated by 45°.

Another scan approach/pattern that can be used is a hexagonal spiral scan, as shown in Figure 8a. The azimuthal step is defined in the same way as for the square scan (14) for the diagonal direction:

$$\Delta Azm = \pm\frac{\varphi_{FRS}}{2}, \quad \Delta El = \pm\frac{\sqrt{3}\varphi_{FRS}}{2}. \tag{16}$$

As a result of these azimuthal and diagonal steps, the coverage/filling of the angular area of uncertainty will increase compared to spiral and square spiral scans. As in the previous method, the points that are outside the scanned area can be removed from the scan, as shown in Figure 8b. However, between the last 3 points, there are relatively long paths, which the gimbal must travel between these points, increasing the scan time. This can be improved by optimizing the scanning order of these points, which is shown in Figure 8c.

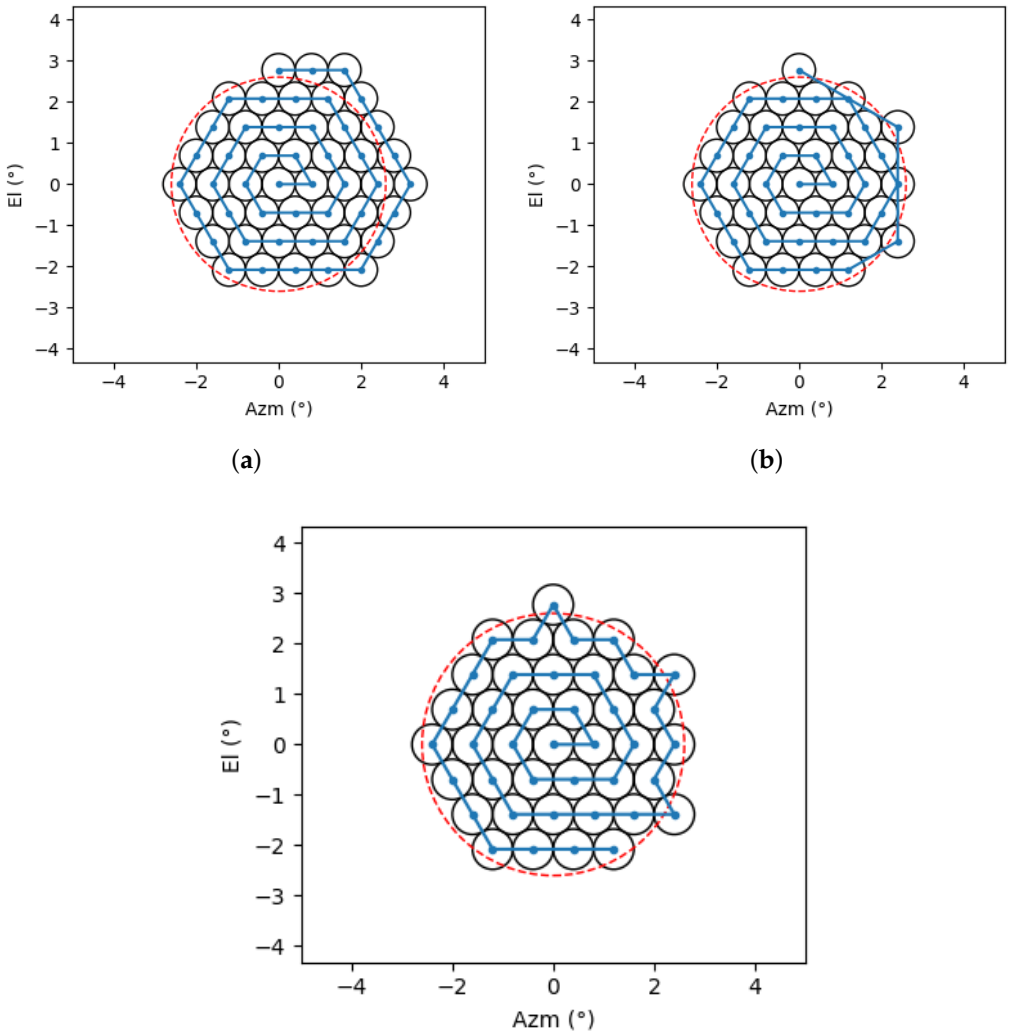

Figure 8. (**a**) Hexagonal spiral scan. (**b**) Cut hexagonal spiral scan. (**c**) Cut hexagonal spiral scan with optimized path.

The time to perform the entire scan can be calculated using the equation

$$T_{scan} = t_{stay} + \sum_{i=0}^{i_{max}-1} \left(t_{move_i} + t_{stay}\right), \tag{17}$$

where t_{stay} is the time required for sample reception and t_{move_i} defines the time required for the gimbal to move from one point to another as

$$t_{move_i} = max\{|Azm_i - Azm_{i+1}|\omega_{Azm}; |El_i - El_{i+1}|\omega_{El}\}, \tag{18}$$

where $|Azm_i - Azm_{i+1}|$ and $|El_i - El_{i+1}|$ define the step in azimuthal and elevational axis and ω_{Azm} and ω_{El} stand for the angular velocity of the azimuthal and elevational axes. For the case where $\omega_{Azm} = \omega_{El}$, the time required for the gimbal to move by a distance of

$$d_{move} = \sqrt{(Azm_i - Azm_{i+1})^2 + (El_i - El_{i+1})^2} \tag{19}$$

will be minimal for case

$$|Azm_i - Azm_{i+1}| = |El_i - El_{i+1}|, \tag{20}$$

which corresponds to diagonal movements.

6. Comparison of Scans for Acquisition

In this section, a comparison will be performed between spiral, cut squared spiral, cut rotated squared spiral by 45°, cut hexagonal spiral, and cut hexagonal spiral with optimized scan path. Two conditions were set for the comparison—the overlap factor F_o was chosen to ensure near 100% coverage of the scanned area and only points with coordinates within an area with a radius of $\Theta_{unc}/2 + \varphi_{FRS}/4$ were considered for the scans. The scan execution time and the number of required points were compared depending on the size of the angular area of uncertainty and the receiver's angle of view. Equation (17) was used with measured movement time data for azimuth and elevational axis, as shown in Figure 9. It can be seen that the movement times for each axis are the same. The gimbal has a function of gradual acceleration and deceleration, which reduces the vibration of the entire optical system when changing the position. The effect of this function can be seen in the graph for smaller changes in the distance angle, where this curve is non-linear. Further time required for sample reception, $t_{stay} = 1$, s was considered for the simulation.

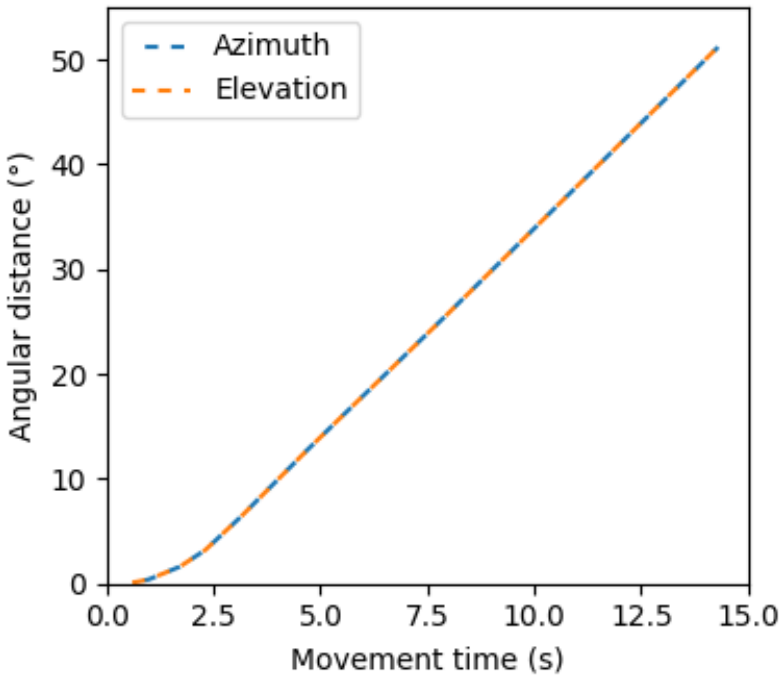

Figure 9. Duration of movement in the azimuthal and elevational directions.

Figure 10 shows a simulation of the required scan time for angular area of uncertainty, Θ_{unc}, in a range of $\langle 4°, 10° \rangle$ and the receiver angle of view, $\Theta_{AOV} = 1°$ (the dependency is shown as a ration of $\Theta_{unc}/\Theta_{AOV}$). As can be seen in Figures 6–8, there are many places within the angular area of uncertainty that are not covered by the scan. The coverage of this area of uncertainty can be expressed by the fill factor, which is given as a percentage and, in the case of complete coverage of the area of uncertainty by scan, reaches a value of 100%. Since each scan pattern shown above achieves a different fill factor value, which is much lower than 100%, the overlap of scan points was set so that the fill factor was higher than 95%. The necessary overlap factor (F_0) for individual methods was set as $F_0 = 0.24$ for spiral scans, $F_0 = 0.33$ for square spiral scans, and $F_0 = 0.12$ for hexagonal

spiral scans. The simulation confirmed that, in the case of using a gimbal with the same angular velocity in the azimuth and elevation directions, it is more beneficial to travel between points in diagonal directions. This effect can be seen in the comparison between the squared spiral scan and the rotated squared spiral scan (orange line vs. green line). The step-like shape of squared and hexagonal spirals is caused by the non-linear addition of points due to the enlargement of the angular area of uncertainty shown in Figure 11. Furthermore, a reduction in scan execution time can be observed for the hexagonal spiral with the optimized path (red line vs. purple line). The scan execution time reduction between cut squared spiral vs. cut rotated squared spiral by 45° and cut hexagonal spiral vs. cut hexagonal spiral with optimized scan path is observable for the cases where t_{move_i} is approximately the same size or smaller than t_{stay}. For other cases, the scan execution time is approximately equal.

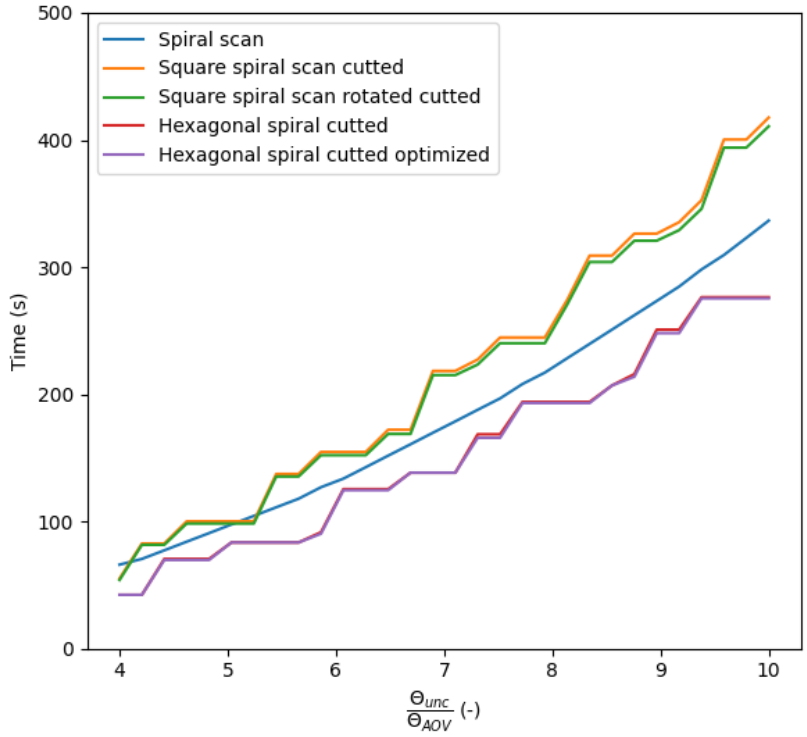

Figure 10. Comparison of scan execution time dependent on the ratio of the angular area of uncertainty and angle of view simulation.

Adequately for the simulation (Figure 10), a real measurement was performed to verify the correctness of the simulation. The transceiver (described in Section 3) based on gimbal Celestron Nexstar Evolution 8 was placed in the university corridor and the Raspberry Pi 4 (which is part of the transceiver) was programmed to move with the gimbal in order to scan the area of uncertainty, Θ_{unc}, in the range of $\langle 4°, 10° \rangle$, where the receiver's angle of view was set to $\Theta_{AOV} = 1°$. Furthermore, the same values of the overlapping factors F_0, as mentioned above, were used, and the time required for sample reception was set to $t_{stay} = 1$ s. At the beginning of the program, the scan points are calculated according to the scanning pattern. Then, the scan starts by sampling data from PSD for time of t_{stay} at the position of the first scan point. This is followed by sending the coordinates of the next point from the Raspberry to the microcontroller, which communicates with the gimbal via an auxiliary port. After this, the Raspberry periodically checks (via the microcontroller) whether the required position has been reached by the gimbal. As soon as the Raspberry determines that the position has been reached, sampling data is performed again for the period of t_{stay}. This procedure is repeated for all scanned points and each scanning pattern. At the beginning and end of each scan, a timestamp was recorded by

which a scan execution time was calculated. A photo of the measurement setup is depicted in Figure 1b. As the transceiver was scanning the whole area of uncertainty (no termination threshold was used), no counterpart transceiver was required for this measurement, and the sampled data from the PSD were not used since the time taken to perform the entire scan is examined. The results of this measurement are shown in Figure 12. The shape of the scan curves obtained by real measurement corresponds to the simulated ones. In general, all scans were performed for a longer time than the simulation was calculated. This was caused by communication for controlling the gimbal (due to the hardware concept) and sampling data from the PSD, which lasted longer than 1 s. This fact was also manifested in the case of the cut square spiral scan which should be slower than the cut rotated square spiral scan (control of only one motor for azimuthal or elevation movement vs. control of both motors for diagonal movement). By performing this measurement, the simulated data presented above can be considered valid, and the same simulation principle can be used for further investigation, such as the one that will follow.

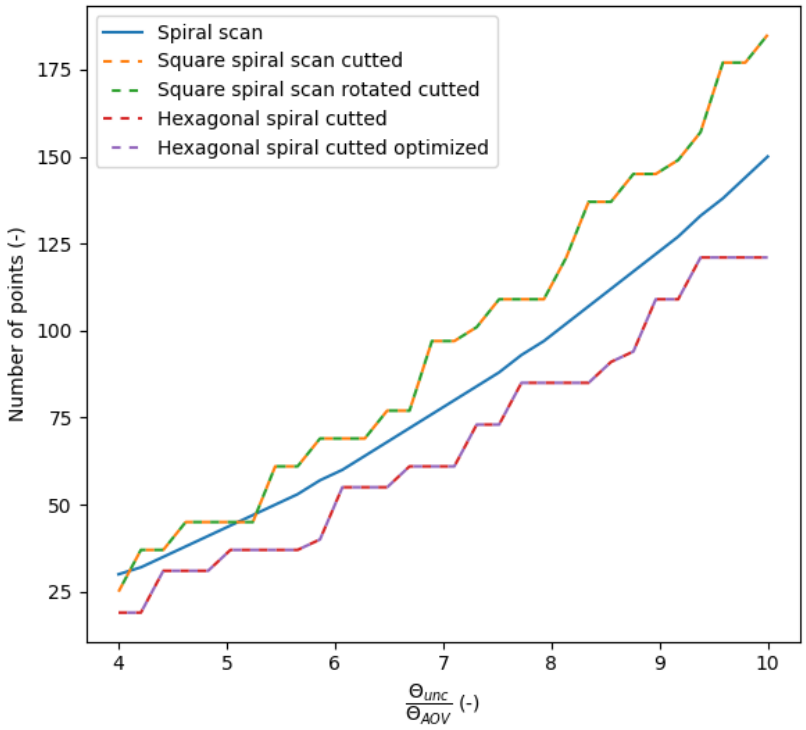

Figure 11. Comparison of the number of points needed to scan the angular area of uncertainty.

The comparison above was based on the time required to perform the entire scan. In real conditions, however, the scan ends when an optical power threshold is exceeded, which speeds up acquisition and pointing. This case was simulated by the sweeping angle between transceivers (angle displacement) in the range of $\sigma = \Theta_{unc}/2$ around the mean value of $\mu = 0°$ by the normal distribution. This generated and averaged 10,000 angle displacements for each angular area of uncertainty, Θ_{unc}, linearly divided into 30 values in the range of $\langle 4°, 10° \rangle$ and the receiver's angle of view, $\Theta_{AOV} = 1°$. Each obtained value was then compared to the scan pattern with the best results (marked as reference) by calculating relative time saving as

$$Relative\_time\_saving = \left(1 - \frac{T_{scan_{reference\_pattern}}}{T_{scan_{pattern}}}\right) * 100 \quad [\%], \tag{21}$$

where $T_{scan_{reference\_pattern}}$ is the execution time of the reference scan pattern and $T_{scan_{pattern}}$ is the execution time of the compared scan pattern. These relative time savings were

then averaged over all obtained values for each Θ_{unc} to obtain an average relative time saving. The result of this simulation is shown in Figure 13, where the scan execution time required to trigger threshold is shown. It can be seen that the cut hexagonal spiral scan achieved the lowest necessary time for the scan and was marked as the reference scan pattern. From this, the relative time saving, for example, of the spiral scan pattern can be calculated at $\frac{\Theta_{unc}}{\Theta_{AOV}} = 8$, where the $T_{scan_{reference\_pattern}} = 51.3$ s (average time required to trigger the threshold in the case of the cut hexagonal spiral scan) and the $T_{scan_{pattern}} = 61.3$ s (average time required to trigger the threshold in the case of the spiral scan) leads to $Relative\_time\_saving = 16.31\%$. The comparison of the scan terminated by exceeding the threshold for all patterns to the cut hexagonal spiral scan is summarized in Table 1. The cut hexagonal spiral scan pattern required, on average, 18.1% less relative time than a spiral pattern and 26.8% less relative time than the cut square spiral pattern. The cut hexagonal spiral scan also achieved better results compared to the cut hexagonal spiral scan with an optimized path (the obtained result is thus opposite to the simulation shown in Figure 10 and real measurement shown in Figure 12, where the effectiveness of the full scan was investigated). This is caused by the fact that, in most cases, the scan is finished much earlier, so the points whose order were modified are not scanned at all, or these "reordered" points cause delayed scanning of points that are in the area with a higher probability of the occurrence of an optical beam (area closer to center of Θ_{unc}), and therefore the scan takes longer than in the case of a scan without an optimized path.

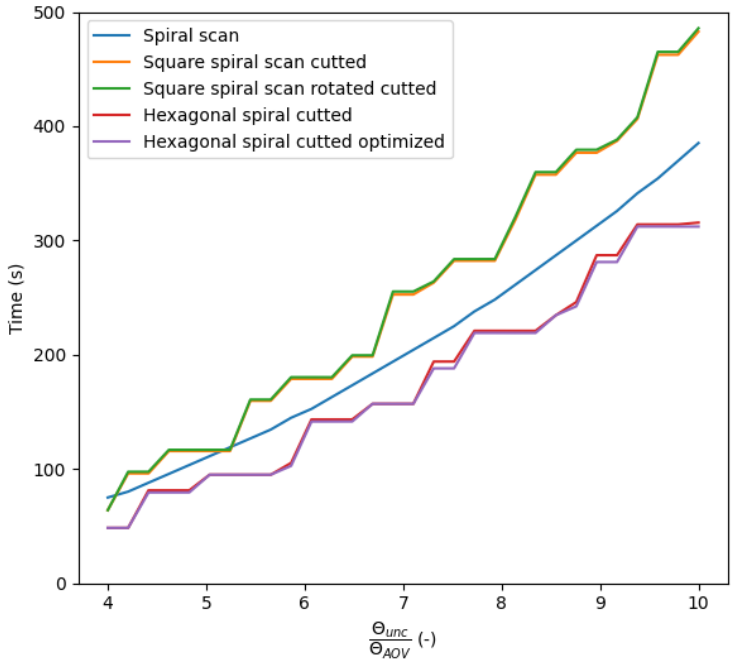

Figure 12. Comparison of scan execution time dependent on the ratio of the angular area of uncertainty and angle of view-real measurement.

Table 1. Average relative time saving for scan terminated by exceeding threshold of cut hexagonal spiral scan compared to all presented patterns.

Type of Scan	Average Relative Time Saving
Spiral	18.1
Cut squared spiral	26.8
Cut rotated squared spiral	22.6
Cut hexagonal spiral with optimized path	0.29

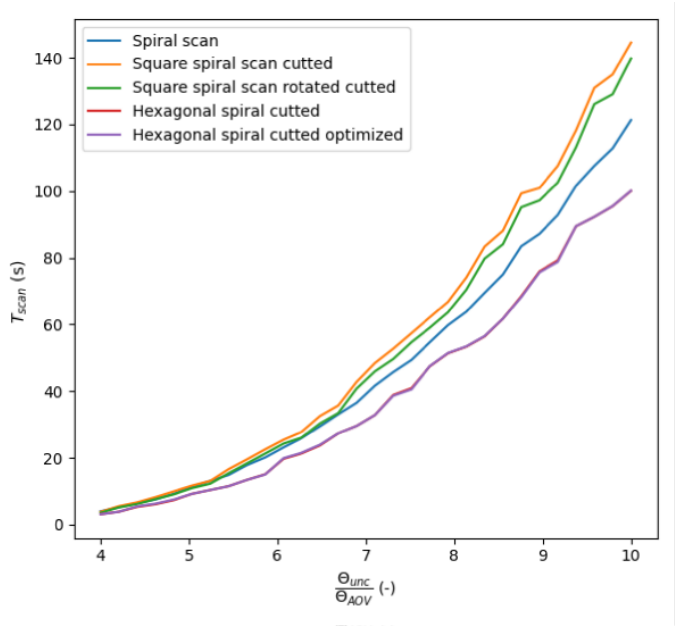

Figure 13. Comparison of scan execution time required to trigger threshold.

7. Conclusions

In this paper, the impact of electro-mechanical parts on the angular area of uncertainty, which has to be scanned, was presented. At short distances (approximately <500 m), the effects of GNSS accuracy and compass accuracy prevail. As the distance increases, the influence of GNSS accuracy decreases and the angular area of uncertainty is mainly given by the compass accuracy. The influence of atmospheric phenomena was neglected, because the purpose of the scan is to capture the optical beam on the PSD sensor roughly. Moreover, these phenomena are suppressed by averaging the optical power for t_{stay}.

Various spiral scan patterns were introduced, simulated, and compared in terms of the time and number of points necessary to cover the complete angular uncertainty area. The simulations and results were presented for a gimbal with equal angular velocity in both the azimuthal and elevation axes. The optimized cut hexagonal spiral scan exhibited the most efficient scanning time. A comparison was then made between this simulation and actual measurements. The recorded values slightly exceeded the simulated results, attributed to system control overhead.

Furthermore, the cut rotated square spiral scan, which was expected to require less time based on simulation, actually demanded slightly more time than the cut square spiral scan. In practical applications, scanning ceases upon surpassing the predefined threshold. This threshold-based termination was applied to all the proposed patterns in the simulations. From this perspective, the cut hexagonal spiral scan achieved an average time reduction of 18.1% compared to the conventional spiral scan and 26.8% compared to the cut square spiral scan. A suitable choice of threshold for terminating the scan can significantly reduce the time required to find the counterpart transceiver.

Author Contributions: Conceptualization, P.S. and P.B.; data curation, P.S.; funding acquisition, P.B.; investigation, P.S. and P.B.; methodology, P.B.; software P.S.; supervision, P.B.; validation, P.B. and P.S.; visualization, P.B.; writing, P.S. and P.B. All authors have read and agreed to the published version of the manuscript.

Funding: This work has been supported by the CESNET FR710/2022 under a grant agreement entitled Phase-coherent transmission of optical frequencies over optical fiber and optical wireless links and by the Internal Grant Agency of the Brno University of Technology FEKT-S-23-8191.

Institutional Review Board Statement: Not applicable.

Informed Consent Statement: Not applicable.

Data Availability Statement: The raw data supporting the conclusions of this article will be made available by the authors on request.

Conflicts of Interest: The authors declare no conflicts of interest.

Abbreviations

The following abbreviations are used in this manuscript:

AAP	Average Acquisition Probability
AI	Artificial Intelligence
AOV	Angle Of View
APT	Acquisition, Pointing and Tracking
CCD	Charge Coupled Device
CMOS	Complementary Metal Oxide Semiconductor
EDFA	Erbium-Doped Fiber Amplifiers
FOV	Field Of View
FSM	Fast-Steering Mirror
FSO	Free-Space Optics
GEO	Geostationary Orbit
GNSS	Global Navigation Satellite System
LEO	Low Earth Orbit
LOS	Line Of Sight
MEMS	Micro-Electromechanical System
PID	Proportional–Integral–Derivative controller
PSD	Position Sensitive Detector
PSO	Particle-Swarm Optimization
RF	Radio Frequency
RTK	Real Time Kinematic

References

1. Next G Alliance Report: 6G Technologies. Available online: https://www.nextgalliance.org/white_papers/6g-technologies/ (accessed on 12 March 2024).
2. Bernardos, C.J.; Uusitalo, M.A. The 5G Infrastructure Association European: European Vision for the 6G Network Ecosystem. Available online: https://zenodo.org/record/5007671 (accessed on 12 March 2024).
3. Manias, D.M.; Javadtalab, A.; Naoum-Sawaya, J.; Shami, A. The Role of Optical Transport Networks in 6G and Beyond: A Vision and Call to Action. *J. Sens. Actuator Netw.* **2023**, *12*, 43. [CrossRef]
4. Dat, P.T.; Kanno, A.; Yamamoto, N.; Kawanishi, T. Seamless convergence of fiber and wireless systems for 5G and beyond networks. *J. Lightwave Technol.* **2019**, *37*, 592–605. [CrossRef]
5. Jeon, H.B.; Kim, S.M.; Moon, H.J.; Kwon, D.H.; Lee, J.W.; Chung, J.M.; Han, S.K.; Chae, C.B.; Alouini, M.S. Free-Space Optical Communications for 6G Wireless Networks: Challenges, Opportunities, and Prototype Validation. *IEEE Commun. Mag.* **2023**, *61*, 116–121. [CrossRef]
6. Saeed, N.; Almorad, H.; Dahrouj, H.; Al-Naffouri, T.Y.; Shamma, J.S.; Alouini, M.S. Point-to-Point Communication in Integrated Satellite-Aerial 6G Networks: State-of-the-Art and Future Challenges. *IEEE Open J. Commun. Soc.* **2021**, *2*, 1505–1525. [CrossRef]
7. Harada, R.; Shibata, N.; Kaneko, S.; Imai, T.; Kani, J.I.; Yoshida, T. Adaptive Beam Divergence for Expanding Range of Link Distance in FSO with Moving Nodes toward 6G. *IEEE Photonics Technol. Lett.* **2022**, *34*, 1061–1064. [CrossRef]
8. Bekkali, A.; Fujita, H.; Hattori, M. New Generation Free-Space Optical Communication Systems with Advanced Optical Beam Stabilizer. *J. Lightwave Technol.* **2022**, *40*, 1509–1518. [CrossRef]
9. Wang, X.; Su, X.; Liu, G.; Han, J.; Wang, K.; Zhu, W. A Method for Improving the Detection Accuracy of the Spot Position of the Four-Quadrant Detector in a Free Space Optical Communication System. *Sensors* **2020**, *20*, 7164 . [CrossRef] [PubMed]
10. Abdelfatah, R.; Alshaer, N.; Ismail, T. A review on pointing, acquisition, and tracking approaches in UAV-based fso communication systems. *Opt. Quantum Electron.* **2022**, *54*, 571. [CrossRef]
11. Park, S.; Yeo, C.I.; Heo, Y.S.; Ryu, J.H.; Kang, H.S.; Kim, S.C.; Jang, J.H. Common path-based mobile free-space optical terminal with adaptive beamforming function for Gbps out-of-band full-duplex connectivity to UAVs. *Opt. Commun.* **2021**, *494*, 127041. [CrossRef]
12. Abadi, M.M.; Cox, M.A.; Alsaigh, R.E.; Viola, S.; Forbes, A.; Lavery, M.P.J. A space division multiplexed free-space-optical communication system that can auto-locate and fully self align with a remote transceiver. *Sci. Rep.* **2019**, *9*, 19687. [CrossRef] [PubMed]

13. Lavery, M.P.J.; Peuntinger, C.; Günthner, K.; Banzer, P.; Elser, D.; Boyd, R.W.; Padgett, M.J.; Marquardt, C.; Leuchs, G. Free-space propagation of high-dimensional structured optical fields in an urban environment. *Sci. Adv.* **2017**, *3*, e1700552. [CrossRef] [PubMed]
14. Ahdi, F.; Subramaniam, S. Optimal placement of FSO relays for network disaster recovery. In Proceedings of the 2013 IEEE International Conference on Communications (ICC), Budapest, Hungary, 9–13 June 2013; pp. 3921–3926. [CrossRef]
15. Kaushal, H.; Jain, V.; Kar, S. Acquisition, Tracking, and Pointing. In *Free Space Optical Communication*; Optical Networks; Springer: New Delhi, India, 2017; pp. 119–137. [CrossRef]
16. Kaymak, Y.; Rojas-Cessa, R.; Feng, J.; Ansari, N.; Zhou, M.; Zhang, T. A Survey on Acquisition, Tracking, and Pointing Mechanisms for Mobile Free-Space Optical Communications. *IEEE Commun. Surv. Tutorials* **2018**, *20*, 1104–1123. [CrossRef]
17. Zhang, M.; Li, B.; Tong, S. A New Composite Spiral Scanning Approach for Beaconless Spatial Acquisition and Experimental Investigation of Robust Tracking Control for Laser Communication System with Disturbance. *IEEE Photonics J.* **2020**, *12*, 7906212. [CrossRef]
18. Li, X.; Yu, S.; Ma, J.; Tan, L. Analytical expression and optimization of spatial acquisition for intersatellite optical communications. *Opt. Express* **2011**, *19*, 2381–2390. [CrossRef] [PubMed]
19. Hudcova, L.; Barcik, P. Experimental measurement of beam wander in the turbulent atmospheric transmission media. In Proceedings of the 22nd International Conference Radioelektronika 2012, Brno, Czech Republic, 17–18 April 2012; pp. 1–4.
20. Coman, C.M.; Tătăroiu, R.; Rosner, D. Autoalignment module for free space laser communications. In Proceedings of the 2013 RoEduNet International Conference 12th Edition: Networking in Education and Research, Constanta, Romania, 26–28 September 2013; pp. 1–6. [CrossRef]
21. Fernandes, M.A.; Brandão, B.T.; Georgieva, P.; Monteiro, P.P.; Guiomar, F.P. Adaptive optical beam alignment and link protection switching for 5G-over-FSO. *Opt. Express* **2021**, *29*, 20136–20149. [CrossRef] [PubMed]
22. Qi, S.; Zhang, Q.; Xin, X.; Tao, Y.; Tian, Q.; Tian, F.; Cao, G.; Shen, Y.; Chen, D.; Gao, Z.; et al. Research on Scanning Method in Satellite Laser Communication. In Proceedings of the 2019 18th International Conference on Optical Communications and Networks (ICOCN), Huangshan, China, 5–8 August 2019; pp. 1–3. [CrossRef]
23. Jia, B.; Jin, F.; Lv, Q.; Li, Y. Improved Target Laser Capture Technology for Hexagonal Honeycomb Scanning. *Photonics* **2023**, *10*, 541. [CrossRef]
24. Rana, M.S.; Pota, H.R.; Petersen, I.R. Spiral Scanning with Improved Control for Faster Imaging of AFM. *IEEE Trans. Nanotechnol.* **2014**, *13*, 541–550. [CrossRef]
25. Moon, H.J.; Chae, C.B.; Wong, K.K.; Alouini, M.S. Pointing-and-Acquisition for Optical Wireless in 6G: From Algorithms to Performance Evaluation. *IEEE Commun. Mag.* **2024**, *62*, 32–38. [CrossRef]
26. Cao, K.; Du, H.; Zhang, J.; Hao, G.; Ran, Q.; Ma, J. Calculation of average acquisition probability for spiral–circular composite scanning in free space optical communication. *Opt. Commun.* **2023**, *532*, 129267. [CrossRef]
27. Zhang, J.; Kane, T.J. Acquisition, tracking, and pointing for reconfigurable free space optical communication systems in RF challenged environments. In *Free-Space Laser Communications XXXII*; Society of Photo-Optical Instrumentation Engineers (SPIE) Conference Series; Hemmati, H., Boroson, D.M., Eds.; SPIE: Bellingham, WA, USA, 2020; Volume 11272, p. 112721L. [CrossRef]